Mitigating the Torque Ripple in Electric Traction using Proportional Integral Resonant Controller

Hawwooi Chuan, Seyed Mahdi Fazeli, Zhongze Wu, *Member, IEEE*, and Richard Burke

Abstract— There is increasing popularity of using permanent magnet (PM) machines in vehicle propulsion systems. Due to the pre-excitation of PM, the machines could offer higher efficiency and torque density. However, their inherent torque ripple could be problematic for electric vehicles (EVs) due to low damping of torsional vibration which may affect passenger comfort. This can prohibit the use of PM machines to improve vehicle energy efficiency. This paper presents the application of resonant control (RC) to suppress the impact of the PM torque ripple, which aims to reduce the vibration of a vehicle. A prototype PM machine and driveline have been fitted to a light-duty off-road vehicle. Firstly, the drivetrain frequency response was analyzed. The main source of the vibration is identified as the 24th harmonic torque ripple of the 12-slot/8-pole PM machine, which originates from the cogging torque and air-gap flux harmonics. The vibration becomes more severe when the torque ripple frequency is close to the natural frequency of the drivetrain. Then, the RC in conjunction with PI controller (PIR) was introduced to be used at the outer speed loop, so that an accurate current reference signal can be generated for the inverter to mitigate the speed ripple. When compared to the conventional Proportional-Integral (PI) controller, PIR controller has demonstrated over 80% reduction in speed ripple, even when the torque ripple frequency is close to the natural frequency of the vehicle.

***Index Terms*—Interior permanent magnet synchronous machine, electric traction, torque ripple, resonant controller.**

I. Introduction

PM machine generally suffers from its inherent cogging torque, which causes speed ripple and the vibration of the coupled components, particularly in the low-speed operation [1]. The vibration is most noticeable by passengers when the vibration frequency is low [2]. The cogging torque will cause a different level of vibration depending on the motor speed, as the powertrain has a nonlinear dynamic response, in which the natural frequency of the powertrain is mainly determined by the half shaft, rotor inertia and vehicle inertia [3]-[5]. In the article published by the Chevrolet Bolt design team [6], they had tried to mitigate the vehicle speed ripple by improving the machine design, but the torque ripple will still be excited at the drivetrain natural frequency, where the typical natural frequency of a drivetrain is 5 – 40 Hz. Whilst improving the mechanical design can certainly reduce the impact of torque ripple, but it may not be sufficient when the vehicle is running at low speed.

In this paper, the focus will be on mitigating the torque ripple at the source by improving the bandwidth of the speed-control loop, where the natural frequency of the drivetrain will also be included in the study. Firstly, a review of relevant literature will be presented in section II. In Section III, the resonant controller is described compared to a traditional Proportional-Integral (PI) controller. Section IV presents the model and experimental facilities used to analyze the RC controller. Then, the natural frequency of the powertrain is studied in Section V. Section VI presents the results for the mitigation of the speed ripple from the model, test rig and on-vehicle. Finally, the conclusions are presented in section VII.

II. Literature Review

The propulsion of electric vehicles (EVs) can be controlled by using either torque control or speed control. The torque control strategy is a more conventional way in propulsion control, as it was used in every internal combustion engine vehicle. Therefore, the accelerator pedal of the early generation of EVs is responsible for sending the torque control signal to the motor control unit. In recent years, vehicle manufacturers, such as BMW and Tesla, had implemented one-pedal driving concept, in which the speed control signal is sent to the control unit based on the position of "accelerator pedal" [7]. One pedal driving could increase the driving efficiency because it can reduce the use of mechanical brake [8].

The summary of the literature for both torque and speed control modes is presented in Fig. 1. Although some of the researches are not specifically designed for electric vehicles where the vehicle dynamic is not considered, the torque ripple compensation method could potentially be used for electric vehicles.

For Chevrolet Bolt, to reduce the speed ripple when the vehicle is running at a low speed, the current command of the motor is shaped by a look-up table, which is a function of the torque command and the rotor position [6]. Meanwhile, Nissan reported that Nissan Leaf had experienced a significant amount

Manuscript received February 19, 2020; revised May 27, 2020 and July 10, 2020; accepted July 28, 2020. Paper no. VT-2020-00608. (*Corresponding Author: Zhongze Wu.*)

Hawwooi Chuan, Seyed Mahdi Fazeli, Zhongze Wu and Richard Burke are with The Institute for Advanced Automotive Propulsion Systems (IAAPS), Department of Mechanical Engineering, University of Bath, Bath, BA2 7AY, United Kingdom (e-mail: hawwooi@yahoo.com, smf50@bath.ac.uk, z.wu@bath.ac.uk, r.d.burke@bath.ac.uk).

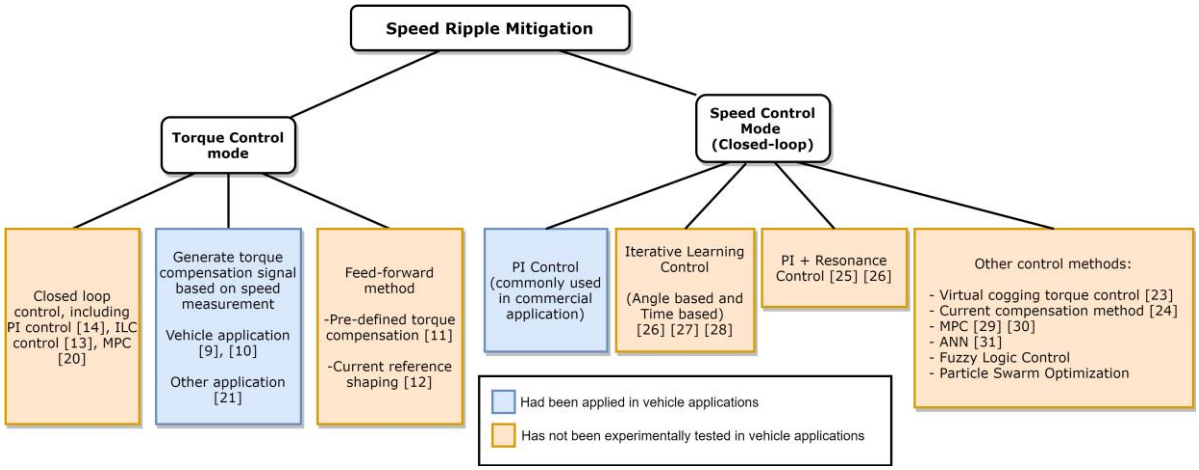

Fig. 1: Summary of the literature in reducing the speed ripple of a motor.

of vibration during acceleration with conventional torque control method [9]. The frequency response of the vehicle was also investigated in the report, where the drivetrain's natural frequency is around 10 Hz. To solve the vibration issue, the speed feedback signal and predefined vehicle dynamic are used to generate the torque compensation signal to reduce the torque ripple. In [10], a similar compensation approach was used on an electric bus to reduce the vibration caused by gear shifting and acceleration, in which the vibration can be reduced by up to 84% during vehicle acceleration and up to 45% during gear shifting.

The methods presented from here onwards are not specifically design for electric vehicle application. In [11], a feedforward method was deployed to reduce the cogging torque based on the offline-measured torque ripple, where the speed ripple can be mitigated by more than 60%. From [12], the authors show the torque ripple caused by flux harmonics can be mitigated by shaping the reference current based on the calculated back-EMF. Nevertheless, feedforward compensation methods are not robust enough, where a little error or parameter change, or disturbance may lead to a larger torque ripple [13].

Another way to reduce the torque ripple is to implement a closed-loop torque control strategy for the drive control. The instantaneous torque can either be measured or estimated, then a controller is used to minimize the error between the measured and reference torque. It was presented in [14] that a torque transducer with a high bandwidth is needed to compensate the torque ripple. However, torque transducers are not usually deployed in commercial products due to costs and the low measurement bandwidth [15]. Therefore, many torque estimation methods were proposed by researchers [16]-[19]. For instance, in [19], the authors had presented that the disturbance torque can be estimated using Kalman filter based on the rotor angle, hence the torque compensation signal can be generated to reduce the disturbance.

For the control strategy used in torque control mode, the use of iterative learning control (ILC) to mitigate the torque ripple is presented in [13]. In ILC, it is effective to reduce the repetitive error, since the error from the previous cycle is used as an input variable to the controller to reduce the error in the current cycle. As model predictive control could take into account the nonlinearities, it was used to solve the vibration problem of an electric bus during acceleration and deceleration in literature [20]. Active torsional damping by using the speed feedback signal to generate the torque compensation method is shown in [21], where the model-based method and bandpass filter method are used. The results show that the model-based method is better in damping the torsional vibration and disturbance rejection, however, every single machine needs to be tuned individually. As an Interior Permanent Magnet Synchronous Machine (IPMSM) is generally operated in a highly saturated condition at a high load, a generic algorithm-based optimization approach is proposed in [22] to improve the torque estimation model, which can be used to calculate the optimum current to reduce torque ripple.

When the motor is controlled in speed mode, there are two control loops in the system, where the speed is controlled at the outer loop and the current is controlled at the inner loop. For both control loops, the PI controller is commonly used, as this is a robust method with a good tracking performance in both steady- and transient- conditions. Nevertheless, due to the vehicle inertia, the PI controller may suffer from a limited bandwidth to mitigate the speed ripple.

One of the methods to solve the limited bandwidth issue of the PI controller is to add a compensation signal to the reference current sent to the inverter. In [23], the authors proposed to mitigate the cogging torque at low speeds by adding the torque compensation signal which is identified by the equilibrium point of the cogging torque. If compared to directly feeding the torque compensation signal, this method is able to reduce the speed ripple by more than 80%. Meanwhile, the literature [24] shows that the speed ripple can be reduced by modifying the reference current from the speed control loop with respect to the identified current disturbance, which is calculated by passing the measured current through a high-pass filter and a weighting factor. The speed ripple can be reduced by more than 50% at the low speed operating region when compared to the PI controller.

Due to the periodic nature of the torque ripple in electrical machines, a small number of authors have attempted to reduce the torque ripple at low speeds using a resonant controller in conjunction with the PI controller (also known as PIR

controller) [25], [26], in which the overall speed ripple can be mitigated by more than 80% with PIR. Meanwhile, similar to the ILC concept for the torque mode control, ILC for speed mode control is proposed to reduce the speed ripple in [27], [28]. A comparison of ILC, PI control, and PIR controller is presented in [26]. The authors had pointed out that the internal models of the ILC are vulnerable to the delay in the high-frequency components in practical situations, which may be harmful to the system stability, especially when it is used in the speed loop control.

There are some advanced control techniques had been implemented to reduce the speed ripple, which include Model Predictive Control (MPC) [29], [30] and Artificial Neural Network (ANN) [31], etc. MPC utilizes the machine model to predict the machine behavior for the finite state of the inverter which shapes the current to reduce the torque ripple. ANN calculates the optimal current in real-time, where the learning capability of ANN could ensure a convergence that reduces the torque ripple. However, these methods require a high computational power, which is not feasible for commercial applications at present. Therefore, these methods are not considered in this paper.

To ensure the effectiveness of these control methods, the reference current has to be accurately tracked in the inner current loop. In [32], the authors had proposed a novel parameters adjustment method for simultaneously tuning the cascaded PI control loops, which can successfully reduce the speed overshoot of the machine. The optimization technique is implemented to find the optimum parameters of the PI controllers by pushing the term Taylor equilibrium point to zero.

PIR controller is selected to be analysed in this paper, as the magnetic core of IPMSMs generally is highly saturated and the torque ripple is also partially contributed by the currents. Thus, this would restrict the performance of the angle based ILC, as the load current may change the magnitude of the torque ripple. Most of the previous research in electric vehicle focused on reducing the vibration when running in torque-control mode, since it is the conventional method in controlling the propulsion power. When running in speed-control mode, the speed ripple reduction techniques proposed by most literature is not specifically for vehicle application, which does not take into account both the drivetrain dynamics and the vehicle inertia. Therefore, to the best knowledge of the authors, there is a knowledge gap in mitigating the speed ripple of a vehicle when the motor is running in speed-control mode, as shown in the summary table in Fig. 1. One of the reasons behind the gap is that the PI controller is expected to be sufficient to reduce the vibration. However, there is sufficient evidences to show that the PI controller may not be a suitable option to reduce the vibration at a low speed for the machine with a high torque ripple, especially when the ripple frequency is close to the natural frequency of the powertrain. Hence, the use of PIR controller on a vehicle is investigated herein to reduce the vehicle speed ripple, where the vehicle dynamics had also been taken into account. Although the analysis was conducted for a IPMSM, this technique can be used for other types of machines including the surface-mounted PM machines, as the main emphasis is to improve the outer speed loop performance which does not vary according to the type of the machines.

III. Resonant Controller Description

Fig. 2 shows the control diagram when the rotor speed of the motor is achieved using a PI controller. In an ideal case, most of the torque ripple can be mitigated when a tighter speed control is used, where the output of the speed-loop PI controller can provide the reference current that compensates the torque ripple. However, the feedback signal delay in a real system would deteriorate the control bandwidth. For instance, a large vehicle inertia would reduce the control bandwidth of the speed controller, as the vehicle inertia can be described as a low pass filter in the torque-speed relationship. In addition, a low pass filter is required for the feedback signal to reduce the measurement noise, which would also cause an additional delay to the feedback signal.

The controller bandwidth can be increased by increasing the proportional. However, this would limit the high-frequency rejection capability, which would lead to the high-frequency vibration that is discussed in Section II. Hence, the resonant control is introduced to create a Proportional-Integral-Resonant (PIR) controller as shown in Fig. 3. The RC can help to increase the controller bandwidth in a particular frequency range, which will prevent the amplification of the noise at a higher frequency. When implementing PIR in the speed loop, the resonance frequency needs to be updated at different rotor frequencies.

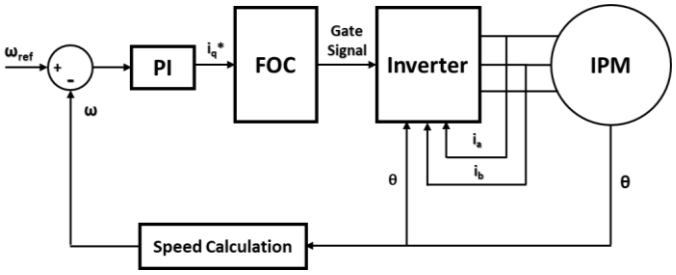

Fig. 2: Speed control with PI controller.

The equation of the combination of PI and resonant controller can be written as [25]:

$$G_{PIR} = K_p + \frac{K_i}{s} + \frac{2K_{RC}\omega_c s}{s^2 + 2\omega_c s + \omega^2} \quad (1)$$

where, ω is the angular frequency of the resonant controller. It is tuned based on the harmonic frequency that the user intends to attenuate. ω_c is the damping coefficient which is the band-wide of ω. K_p, K_i, K_{RC} are the proportional, integral, and resonant controller gains, respectively.

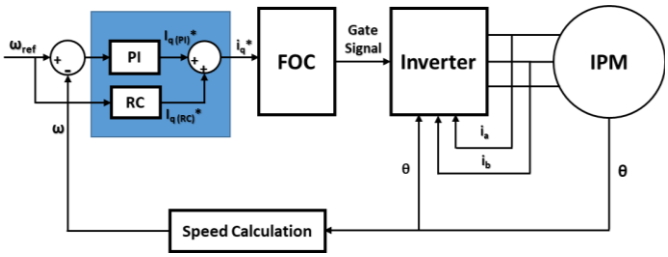

Fig. 3: Speed control with PIR.

IV. MODELLING AND EXPERIMENTAL CONFIGURATION

This section will firstly describe a model of the driveline used to analyze the effectiveness of the PIR controller. Secondly, the experimental configurations will be presented.

A. Dynamic Model of IPMSM and Driveline

The model of the IPMSM and driveline is implemented in MATLAB/Simulink. The voltage equation of an IPMSM in the synchronous reference frame can be written as [33],

$$\begin{bmatrix} v_d \\ v_q \end{bmatrix} = \begin{bmatrix} R_s + pL_d & -\omega_r L_q \\ \omega_r L_d & R_s + pL_d \end{bmatrix} \begin{bmatrix} i_d \\ i_q \end{bmatrix} + \begin{bmatrix} 0 \\ \omega_r \varphi_{PM} \end{bmatrix} \quad (2)$$

where v_d and v_q are the d- and q-axis voltages, respectively. i_d and i_q are the d- and q- axis currents, respectively. L_d and L_q are the d- and q-axis inductances, respectively. R_s is the stator resistance. ω_r is the rotor angular velocity. φ_{PM} is the PM flux linkage. From (2), the motor electromagnetic torque T_e and the motor dynamics can be derived as,

$$T_e = \frac{3}{2} p_n \left[\varphi_{PM} i_q + (L_d - L_q) i_d i_q \right] \quad (3)$$

and

$$J \frac{d\omega_m}{dt} = T_e - T_L \quad (4)$$

where ω_m is the rotor angular velocity, T_L is the load torque, J is the inertia of the motor and load, p_n is the rotor pole-pair number.

B. Maximum Torque Per Ampere (MTPA)

As shown in (3), there are two torque components including both the electromagnetic torque and the reluctance torque. Fig. 4 shows the relationship between d- and q-axis currents for the test IPMSM to produce the desired torque, in which the parameters for the IPMSM are shown in Table 2.

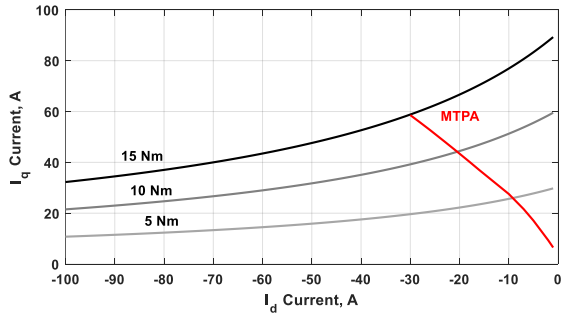

Fig. 4: I_d and I_q current combination for different torque (without consideration of saturation effect).

To achieve the maximum torque per ampere (MTPA), the d- and q-axis currents can be controlled based on the torque demand signal [34], which in this case is the output of the PI controller of the speed control loop. When the saturation effect and the cross-coupling effect are not considered, the q- and d-axis currents can be found by numerically solving (3) and (5) [34], while the MTPA curve of the IPMSM is shown in Fig. 4.

$$I_d = \frac{\varphi_{PM}}{2(L_q - L_d)} - \sqrt{\frac{\varphi_{PM}^2}{4(L_q - L_d)^2} + I_q^2} \quad (5)$$

The variables L_d, L_q and φ_{PM} are not constant, which will vary with core saturation, cross-coupling effect, and temperature [35]. In [36], the authors had shown that the flux linkage and the q-axis inductance of the IPMSM at rated current could drop by 15% and 30%, respectively, where the reduction is close to a linear function. The change of flux linkage and inductance will affect the MTPA operating point selection.

To investigate the impact of MTPA on our test IPMSM, a cross-checking on the saturation effect is performed, which is shown in Fig. 5. It is assumed that the saturation of q-axis inductance and flux linkage are similar to [36], while the cross saturation effect and the change of d-axis inductance are neglected.

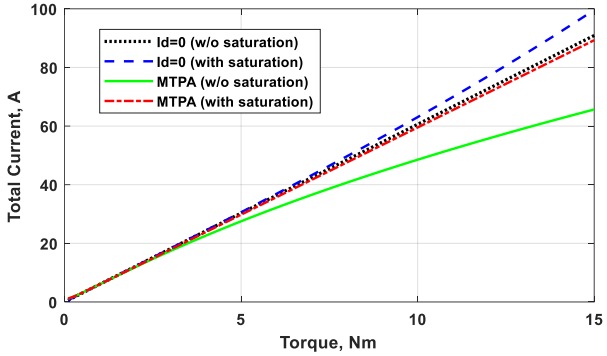

Fig. 5: Comparison between I_d = 0 method with MTPA method.

Fig. 5 shows that when saturation effect is taken into account, the MTPA does not show a significant reduction of current even at a full load, i.e. 15 Nm, where the current can only be reduced by 10%. This is because the saliency ratio L_q/L_d of the test IPMSM is only 2. So, when the saturation effect is taken into account, the saliency ratio would be further reduced at a high current, due to the reduction of L_q.

In addition, it is worth noting that the current difference between both methods is small at a low torque (<5 Nm). In our test vehicle, a 15:1 gearbox ratio is used. Hence, the average motor torque of 5 Nm is used in the test, which is only 1/3 of the rated torque 15 Nm. This means the MTPA method will not be effective in this application. Therefore, the reluctance torque is not considered in this paper, where the d-axis current is assumed to be zero for simplicity, i.e. I_d=0, since improving the outer speed loop controller bandwidth is the main objective of this paper.

C. Torque ripple

1) Cogging Torque

Cogging torque is caused by the attraction force between PMs and stator teeth. It would present even when the stator windings are not excited. The harmonics of the cogging torque can be found as the lowest common multiplier (LCM) of the number of stator slots Q and the rotor pole pair number p, so the cogging torque of the 12-slot/8-pole IPMSM is under the 24th harmonic group of the rotor speed. The cogging torque T_{cog} can be written as [13],

$$T_{cog} = \sum_{n=1}^{\infty} \overline{T_n} \cos(24\, n\theta_m + \alpha_n) \quad (6)$$

where $\overline{T_n}$ and α_n are the magnitude and initial phase angle of the $(24n)^{th}$ cogging torque harmonic, respectively. θ_m is the rotor mechanical angle which is a function of time and rotational speed. As the focus of this paper is to solve the low speed and low torque problem in EV, cogging torque is the main contributor of the torque ripple in the machine.

2) Air-gap Flux Harmonics

The presence of air-gap flux harmonics would produce additional torque ripple in an electrical machine, which is mainly due to the interaction of the fundamental flux harmonics with the higher harmonic order of 5, 7, 11, 13, etc. For a three-phase machine, the torque ripple caused by flux harmonics comes from the 6th harmonic group, which can be expressed as

$$\Delta T_{fh} = T_6 \cos 6\theta_e + T_{12} \cos 12\theta_e + \cdots \quad (7)$$

where θ_e is the rotor electrical angle, T_6 and T_{12} are the peak of the 6^{th} and 12^{th} harmonics torque ripple. For a 4-pole-pair machine, the 6^{th} harmonic at electrical frequency is equivalent to the 24^{th} harmonic torque ripple, which has the same harmonic order as the cogging torque. As the magnitude of the torque ripple caused by flux harmonics is proportional to the stator current, it is negligible when the machine is under a light loaded.

3) Current Measurement Error

The current measurement error can be separated as the DC-offset error and the scaling error. The DC-offset error is caused by the unbalanced DC supply voltage in the current sensors and inherent offset in the analog sensors [13]. Meanwhile, as the output of the current sensor needs to be scaled to match the input of the Analogue-to-Digital (ADC), wrongly tuned current measurement may lead to the scaling error [37].

Assuming ideal current tracking and two of the three-phase currents are measured, the torque ripple due to the current offset error ΔT_{off} and scaling error ΔT_{scale} can be derived as (8) and (9), respectively [13].

$$\Delta T_{off} = \frac{2}{\sqrt{3}} k_t \cos(\theta_e + \delta)\ I \sqrt{\Delta {i_a}^2 + \Delta i_a \Delta i_b + \Delta {i_b}^2} \quad (8)$$

$$\Delta T_{scale} = \left(\frac{K_a - K_b}{K_a K_b}\right) k_t \frac{I}{\sqrt{3}} \left[\cos\left(2\theta_e + \frac{\pi}{3}\right) + \frac{1}{2}\right] \quad (9)$$

where k_t is the machine torque constant, Δi_a and Δi_b are the DC-current offset for phase A and phase B, respectively, K_a and K_b are the scaling of the current for phase A and phase B, respectively.

As shown in (8), the DC current offset will lead to one torque pulsation for every electrical period, and the scaling error will cause two torque pulsations for every electric period. Hence, for a 4-pole-pair machine, DC-offset error and current scaling error will cause 4^{th} and 8^{th} torque ripple harmonics, respectively.

D. Driveline Model

It was shown in [38] that a two-mass damper-spring model is enough to study the frequency response of the powertrain at the low frequency. As this paper focuses on the vehicle in the low-speed region, a two-mass damper-spring model is built to find the lowest natural frequency, where the representation of the two-mass damper-spring model is present in Fig. 6 and the parameters are shown in Table 1.

Equivalent shaft length is used because the half shafts from both sides have different lengths and they are connected through a differential.

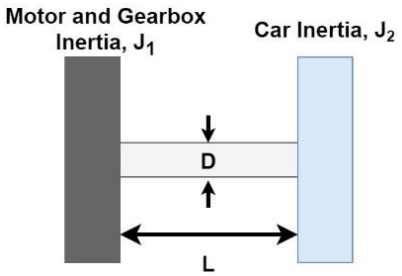

Fig. 6: Two Mass Spring-Damper System.

Table 1: Vehicle and Driveline parameters

Description	Value
Gearbox gear ratio	15:1
Motor inertia, J_1	0.005 kgm^2
Gearbox inertia	0.004 kgm^2
Vehicle inertia, J_2	200 kgm^2
Equivalent Shaft Length, L	0.23 m
Shaft material	Cast Steel
Modulus rigidity of steel, G	78 GPa
Diameter of low speed shaft, D	22 mm

The natural frequency of drivetrain can be calculated using the following equation [39]:

$$f = \frac{1}{2\pi} \sqrt{\frac{\pi G D^4 (J_1 + J_2)}{32 L J_1 J_2}} \quad (10)$$

where, G is the modulus rigidity of the material, L and D are the length and the diameter of the shaft, respectively, J_1 and J_2 are the motor inertia and the vehicle inertia, respectively.

When substituting the parameters shown in Table 1 into (10), the torsional vibration natural frequency of the half shaft can be obtained as f =10 Hz. This will be validated in the following section.

E. Machine and Controller Parameters

The test machine is an IPMSM, which is used to provide propulsion for the vehicle. The IPMSM has a low rated voltage and a high rated current, so the inductance of the machine is relatively low. The parameters for the test machine are presented in Table 2, while the controller parameters are shown in Table 3.

Table 2: Machine Parameters

Description	Value
Slot number, Q	12
Pole number, $2p_n$	8
d-axis inductance, L_d	0.05 mH
q-axis inductance, L_q	0.1 mH
Rated voltage	48 V
Rated RMS current	100 A
Rated torque	15 Nm
Rated speed	3000 RPM

Table 3: Controller Parameters

Description	Value
Proportional gain, K_{sp} (Speed controller)	30
Integral gain, K_{si} (Speed controller)	250
Proportional gain, K_{ip} (Current controller)	40
Integral gain, K_{ii} (Current controller)	6000
Resonance gain, K_{RC} (Speed controller)	120

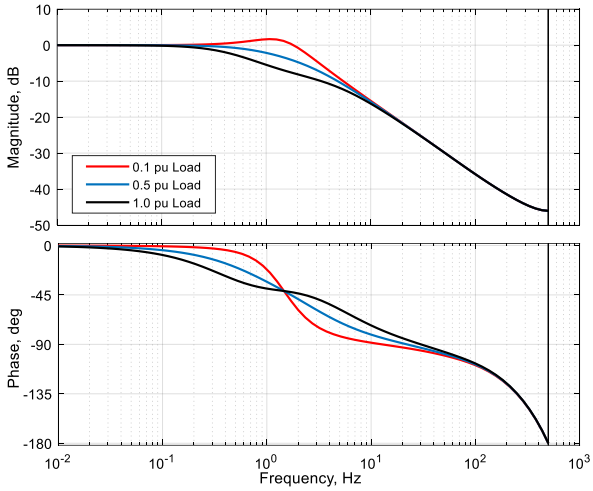

Fig. 7: Frequency response at different loads and PI gains.

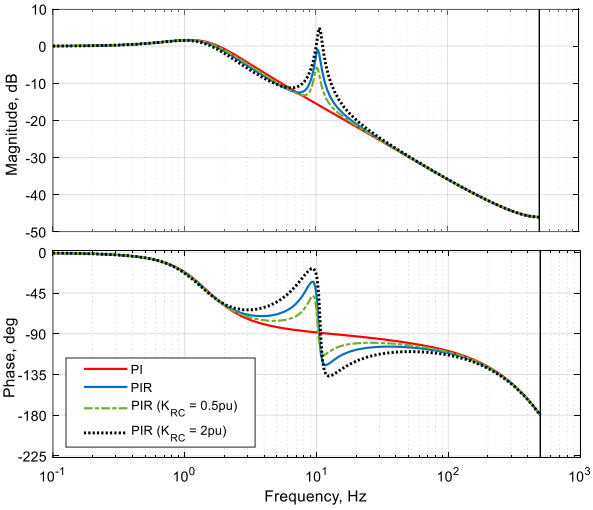

Fig. 8: Frequency response at different resonance gains.

On choosing the PI controller parameters, there is a significant difference between choosing the PI controller in an ideal system and the real scenario. The existence of noise in the real system would limit the bandwidth choice, where the noise could come from the uncontrolled mechanical or electrical source, such as machine vibration, encoder vibration or electromagnetic interference [40]. Therefore, the PI controller of both current and speed loops were tuned using the Ziegler-Nichols method [41], which is an empirical method. As the focus of this paper is to control the outer speed loop, the following discussion will be focusing on the speed loop control.

Firstly, the integral gain is set to zero, and the proportional gain is increased to the point before the speed of the motor goes unstable. From the test, the oscillation period T_u and the maximum gain K_u, are extracted from the measurement, and used in the Ziegler-Nichols method to find the speed loop proportional gain K_{sp} and speed loop integral gain K_{si} as shown in (11) and (12) [41]:

$$K_{sp} = 0.45\, K_u \tag{11}$$

$$K_{si} = 0.54 K_u / T_u \tag{12}$$

Fig. 7 shows the system response changes with the load. For vehicle applications, the load is a function of speed, where an increase of load would also mean that the damping coefficient of the transfer function increases. Therefore, to prevent the overshoot during transient response at any loading condition, it is important to tune the controller when the motor is lightly loaded which has a low damping coefficient.

Regarding the selection of the gain for the resonance controller, a higher resonance gain may cause the system goes unstable, but a lower gain value may cause insufficient response at the specific frequency (see Fig. 8). Therefore, it is recommended that the K_{RC} does not exceed 0 dB at the natural frequency of the vehicle (10 Hz), to prevent the amplification of vibration at the vehicle natural frequency.

F. Experimental Configuration

The motor controller was tested both on a dynamometer facility and within the test vehicle. The experimental setup on the dyno is presented in Fig. 9(b). The dynamometer is an induction machine controlled with a separate system. The load of the test motor can be defined by controlling the torque of the dynamometer. For the control of the test motor, FPGA-based controller (NI-9683 Single-Board RIO) is used to control the inverter. The PI and PIR controllers described in section III are implemented onto this rapid prototyping system. Also, the FPGA controller is used to acquire the measurement data. Field Oriented Control (FOC) was implemented to drive the motor, where the Space Vector Pulse Width Modulation (SVPWM) technique was deployed, and the switching frequency is set at 20 kHz. The DC-bus voltage is provided by a battery emulator.

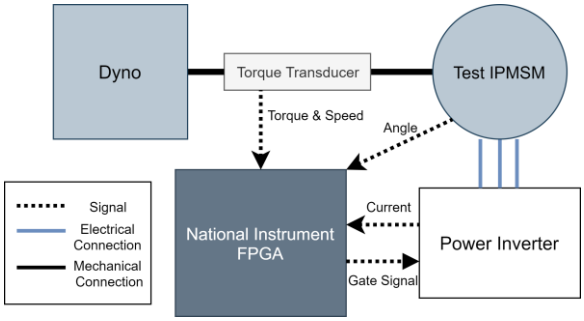

(a)

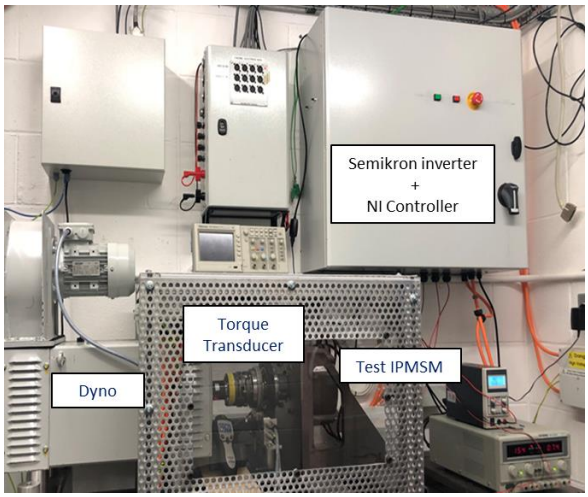

(b)

Fig. 9: Test rig at the University of Bath: (a) Overview (b) Setup.

A mobile version of the rapid-prototyping system was implemented on the test vehicle itself. This follows the same layout as that described in Fig. 9(a), however, the power source is now obtained from the vehicle's battery pack. The test setup is pictured in Fig. 10.

The vibration of the vehicle was measured by using an accelerometer (Dewetron DS-IMU2) with a sampling rate of 100 Hz. The motor is running in speed-control mode, where the speed is controlled with PI controller. Then, the accelerator pedal is replaced with a knob to ensure the vehicle is running at a fixed speed.

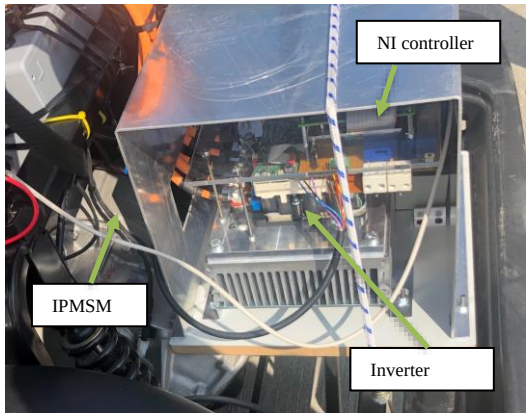

Fig. 10: On-vehicle implementation of the tapir-prototyping controller.

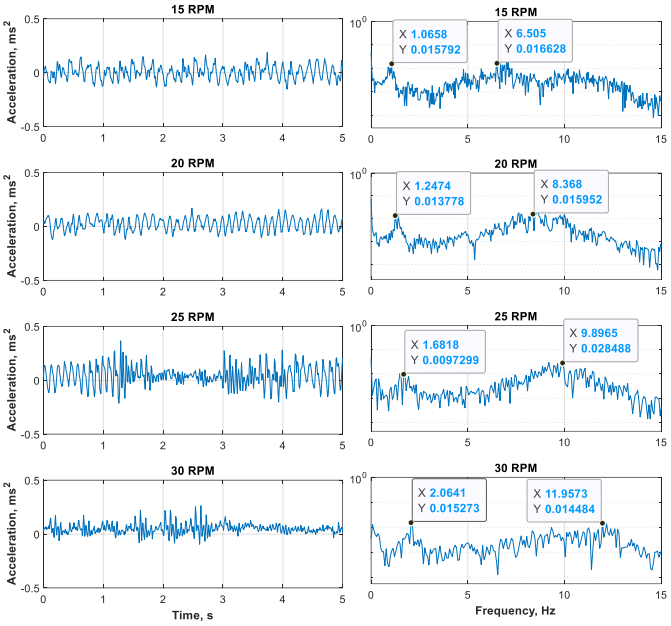

(a) (b)

Fig. 11: Measurements from the accelerometer from 15 to 30 RPM in (a) Time-domain (b) Frequency domain.

V. Baseline Powertrain Analysis

A typical electric powertrain includes an electric motor, a gearbox and a half shaft [42]. This section is to investigate the natural frequency of the powertrain, and the results are validated using the measurement results from the accelerometer installed on the vehicle application. As passenger is less sensitive to speed ripple that higher than 15 Hz [2], only steady-state low-speed and low-load operation are focused here.

From Fig. 11, it shows that the vibration frequency can be separated into two groups. The vibration frequency is a function of rotor frequency because the frequency increases as the rotor speed increases. The two main vibration frequency has the same frequency as the 4^{th} and 24^{th} harmonic of the rotor rotational frequency. As analyzed in Section II, the 4^{th} harmonic torque ripple is due to the DC-measurement offset error, whilst the 24^{th} harmonic torque ripple may be due to the air-gap flux density harmonics and cogging torque of the IPMSM.

Although the magnitude of the IPMSM's torque ripple is almost constant at different rotational speeds, this is not the case when it is used to drive the vehicle, as shown in Table 4. This is because the damping of the torque ripple is lower when the torque ripple frequency is close to the natural frequency of the vehicle's drivetrain. Here, it has shown that the highest vibration occurs when the rotor is running at 25 RPM.

When the rotor speed is 25 RPM, the 24^{th} harmonic torque ripple would cause the speed ripple at 10 Hz, which is close to the calculated natural frequency from the equation (10). Hence, it can be deduced that the torsional vibration of the half shaft is the main contributor to the non-linear vibration characteristic in the vehicle.

Table 4: Summary of Accelerometer Measurements from 15-30 RPM

Rotor (RPM)	4th	24th
	Vibration (m s^{-2})	Vibration (m s^{-2})
15 (0.25 Hz)	0.016	0.016
20 (0.33 Hz)	0.014	0.016
25 (0.42 Hz)	0.010	**0.028**
30 (0.5 Hz)	0.015	0.014

VI. Speed Ripple Mitigation

Due to the existence of measurement, mechanical and electromagnetic noises, increasing the bandwidth through increasing the proportional gain of the controller would lead to a higher frequency vibration. This scenario is shown in Fig. 12, where the vibration increases when the proportional gain is increased. Although the 10 Hz vibration (24th harmonic) can be reduced when the proportional gain increased, the higher frequency vibration had been greatly increased.

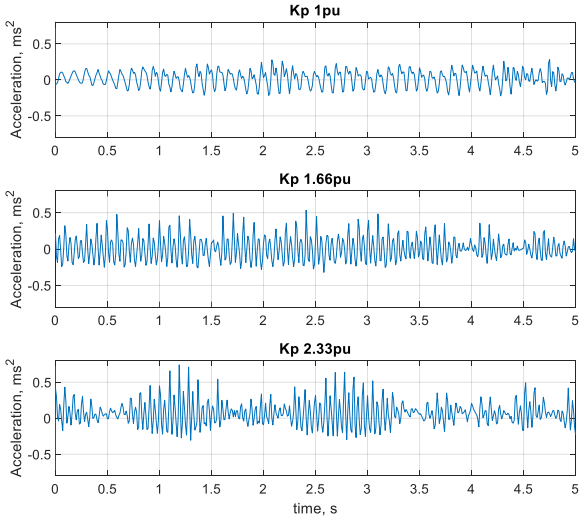

Fig. 12: Vibration measurement for different gain at 25 RPM.

A. Analytical Comparison of PI and PIR Controllers

Due to the implementation of PI-control with a tighter gain could not reduce the vibration problem in the vehicle, PIR controller is investigated in this section.

As the 4th harmonic torque ripple is caused by current measurement offset error, this can be compensated by setting an accurate current measurement offset, so this torque ripple is not considered in further analysis. This measurement error may be a problem for a low-voltage high-current machine because of the wide measurement range of the current sensor. In our case, the current sensor of 900 A is used and the Analog-to-Digital Converter (ADC) board for our NI-controller is 12-bits. Hence, the quantization steps for the current measurement is 0.45 A (1800A / 4096). Hence, to find the accurate measurement offset, the current needs to be measured with another lower rated current sensor.

Furthermore, to increase the closed-loop response, the original encoder sampling time of 5 ms is reduced to 1 ms. The difference between 2 different sampling rates is also investigated in this section.

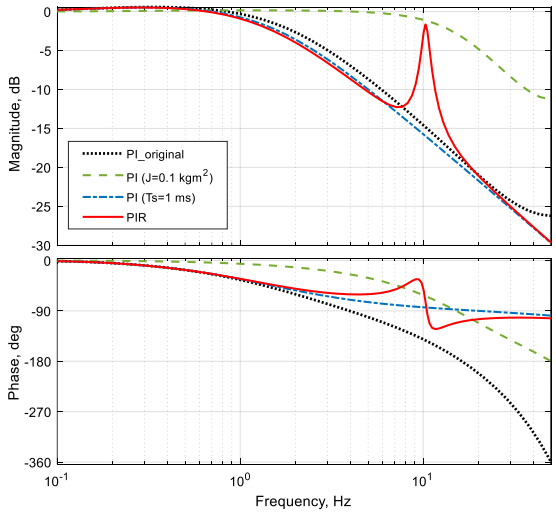

Fig. 13: Closed-loop response at 25 RPM rotor speed.

The closed-loop responses of the PI and PIR controller are comparatively presented in Fig. 13, with consideration of the vehicle inertia. It has shown PIR can increase the bandwidth of certain frequencies. Meanwhile, the PI controllers with different sampling frequencies are also compared, where the original sampling time is 5 ms, and the upgraded sampling frequency is 1 ms. The main difference between both sampling frequencies is the phase difference of low sampling frequency becomes bigger for frequency above 2 Hz. Furthermore, comparing the response of the vehicle reflected inertia (0.89 kg m^2) with the inertia of 0.1 kg m^2, it shows that the increase of inertia would reduce the controller bandwidth, since the vehicle inertia acts as a low-pass filter.

The MATLAB/Simulink model is used to investigate the PI and PIR control methods based on the parameters of the machines and inverter shown in Table 3. Also, the torsional vibration's natural frequency of the half shaft is considered in the model. From Fig. 14, it has shown that the speed ripple can be mitigated when switching from the conventional method to the PIR control method.

Due to the natural frequency of the powertrain, the speed ripple at 25 RPM is higher than 15 RPM when only the PI controller is used. Although the PI controller can produce the reference current that compensates the speed ripple, the compensation is not as effective as the resonance controller, due to the limited controller bandwidth. In Fig. 14(b), although the PI controller's reference current before turning on the RC is almost the same as the RC controller's reference current, the phase shift of RC reference signal can help in mitigating the speed ripple.

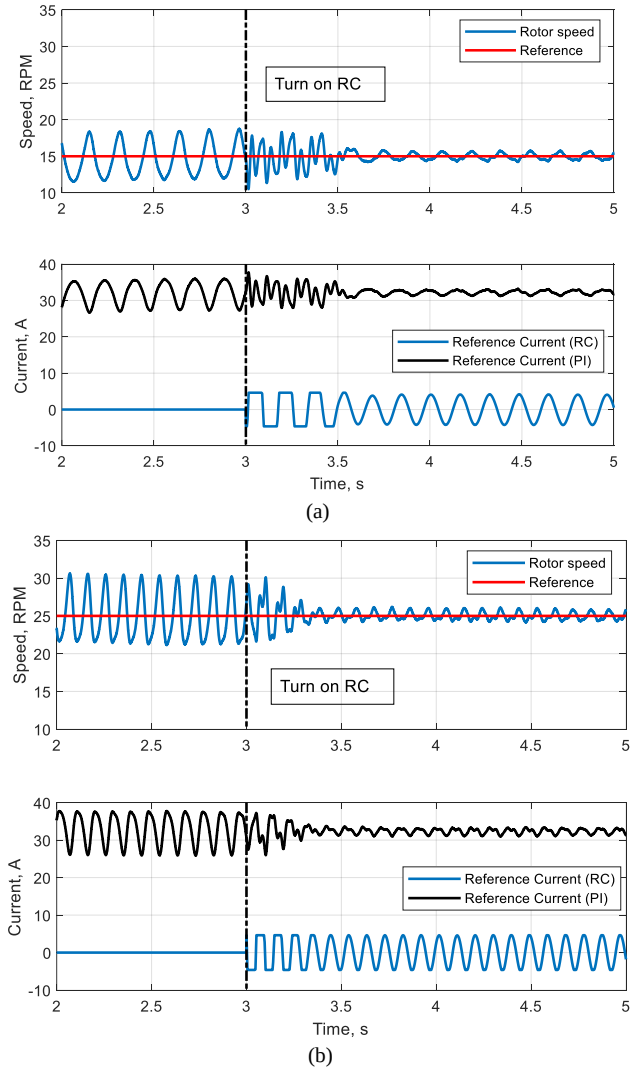

Fig. 14: Simulation results comparison between PI and PIR controller at (a) 15 RPM, (b) 25 RPM.

When added to the PI controller, the resonance controller generates the majority of the reference current signal to compensate the torque ripple, while the PI controller generates the reference signal of the load. Moreover, the speed ripple for both speeds can be mitigated after implementing the resonance controller.

Fig. 15 shows the transient performance of the vehicle ramping up from 0 to 15 RPM and 25 RPM. In the simulation, the frequency of the resonance controller is set to the 24th harmonic of the target rotational frequency, which does not change during the ramp-up. For example, the resonance controller is set to 6 Hz for the reference speed of 15 RPM (0.25 Hz). The reference speed cannot be perfectly tracked in transient, due to the limited bandwidth at a high frequency, which can also be seen in the closed-loop response in Fig. 13 that the response reduces at a high frequency. During the ramp-up, both controllers show similar performance when the difference between reference speed and rotor speed is larger than 20%.

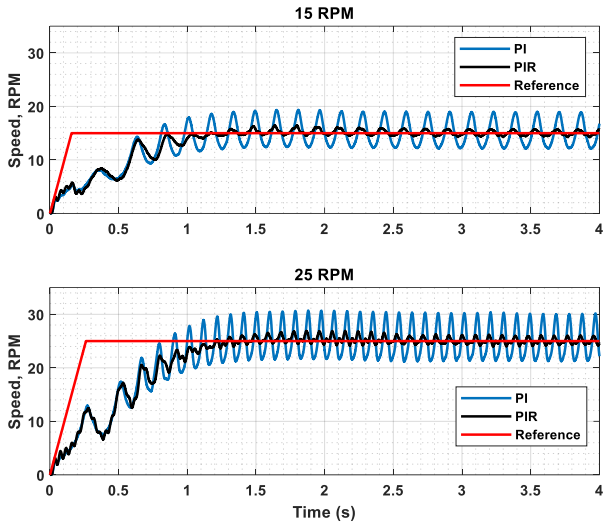

Fig. 15: Transient performance for PI and PIR controllers.

Since the passenger is sensitive to the vibration below 15 Hz, only low-speed operation will be investigated. For instance, 25 RPM rotor speed is equal to 1.67 RPM wheel speed as a 15:1 gear ratio was used, which means the torque of the machine would be sufficient to ramp the speed up in less than one second (see Fig. 15). Therefore, transient performance will not be further tested.

B. Test Rig Verification

As shown in Fig. 16, the IPMSM is tested at 15 RPM, where 6 Hz is the 24th harmonic torque ripple frequency. For the PI controller, when the sampling time is reduced to 1 ms, the speed ripple can be slightly reduced by 24%. If PIR is used at the outer speed control loop, the magnitude of the 6 Hz speed ripple can be further reduced by 64%.

C. On-Vehicle Verification

Both PI and PIR control strategies are implemented on the test vehicle.

The rotor speed measurements when the reference speed is set at 15 RPM and 25 RPM are presented in Fig. 17 and Fig. 18 respectively. Although the existence of vehicle inertia could smoothen the torque ripple, the vehicle inertia would incur delay in the torque-speed response when the outer speed loop is controlled from the speed measurement feedback. Hence, from Table 5, the speed ripple for both control strategies is much higher than the test tested on the test rig.

For the speed ripple mitigation part, similar to the test on the test rig, reducing the encoder sampling will only slightly reduce the speed ripple. When the PIR controller is used, the speed ripple can be reduced by ~83%, even when the speed ripple is close to the natural frequency of the vehicle. This had proven that the PIR can effectively reduce the speed ripple at certain frequencies, where the frequency of the RC needs to be varied based on the reference speed. However, the speed ripple cannot be further reduced with this method because of the phase delay of the RC controller, as shown in the Bode plot in Fig. 13.

Table 5: Summary of the test rig and on-vehicle test results

Operating Condition	24th harmonic speed ripple				
	PI (T_s=5 ms)	PI (T_s=1ms)		PIR	
	Speed ripple (RPM)	Speed ripple (RPM)	Reduction	Speed ripple (RPM)	Reduction
Test Rig (15 RPM)	0.85	0.65	24%	0.10	88%
On-vehicle (15 RPM)	3.18	2.24	30%	0.55	83%
On-vehicle (25 RPM)	4.90	3.90	20%	0.85	83%

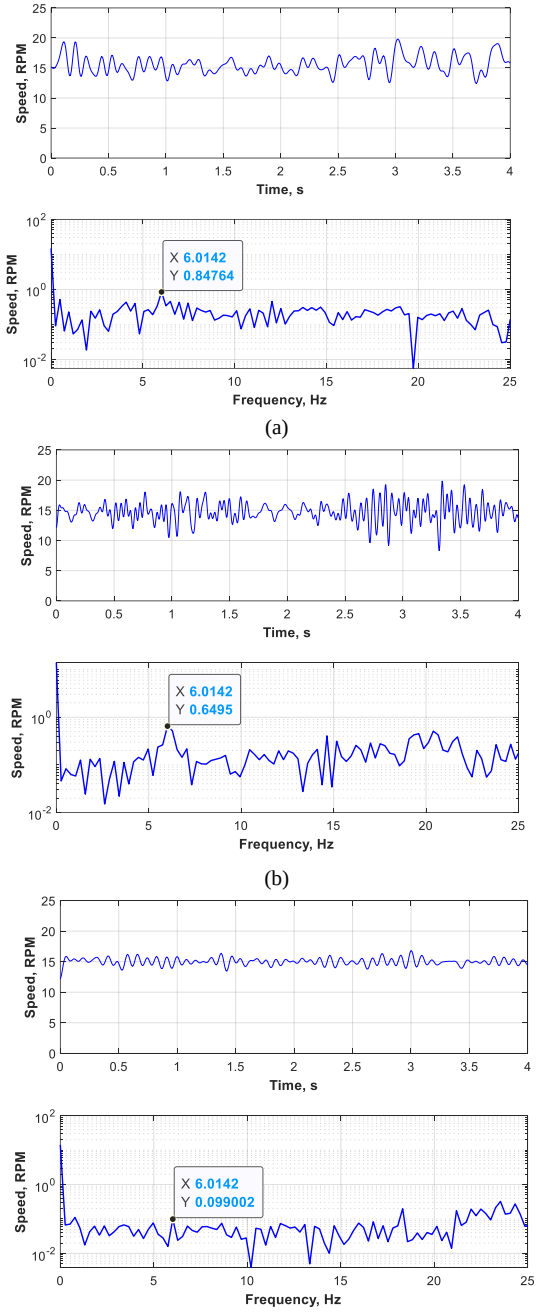

Fig. 16: Speed measurement at 15 RPM with 5 Nm average torque on test rig: (a) PI (T_s = 5 ms), (b) PI (T_s = 1 ms), (c) PIR Controller.

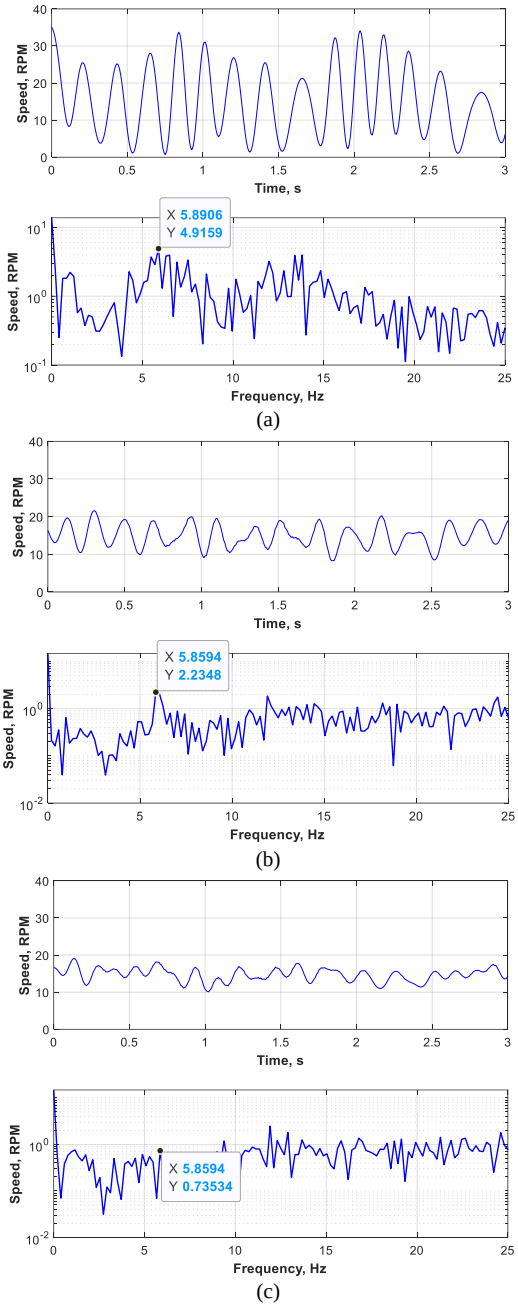

Fig. 17: Speed measurement at 15 RPM with 5 Nm average torque (on-vehicle) : (a) PI (T_s = 5 ms), (b) PI (T_s = 1 ms), (c) PIR Controller.

VII. Conclusion

This paper has highlighted the vibration and comfort problem for vehicles equipped with PM electric machines. The vibration is mainly due to the inherent cogging torque of the PM machine. As vehicle inertia would reduce the speed controller bandwidth, a conventional PI controller is not sufficient to reduce the speed ripple when the motor is running at a very low speed. The resonance controller, coupled with a PI controller, has been shown to reduce the speed ripple of the vehicle by 83% compared to the conventional PI controller. This percentage of reduction is close to the 80% speed ripple reduction shown in literature [25], which uses the PIR controller in a lab-based testing with relatively low inertia and without considering vehicle dynamic.

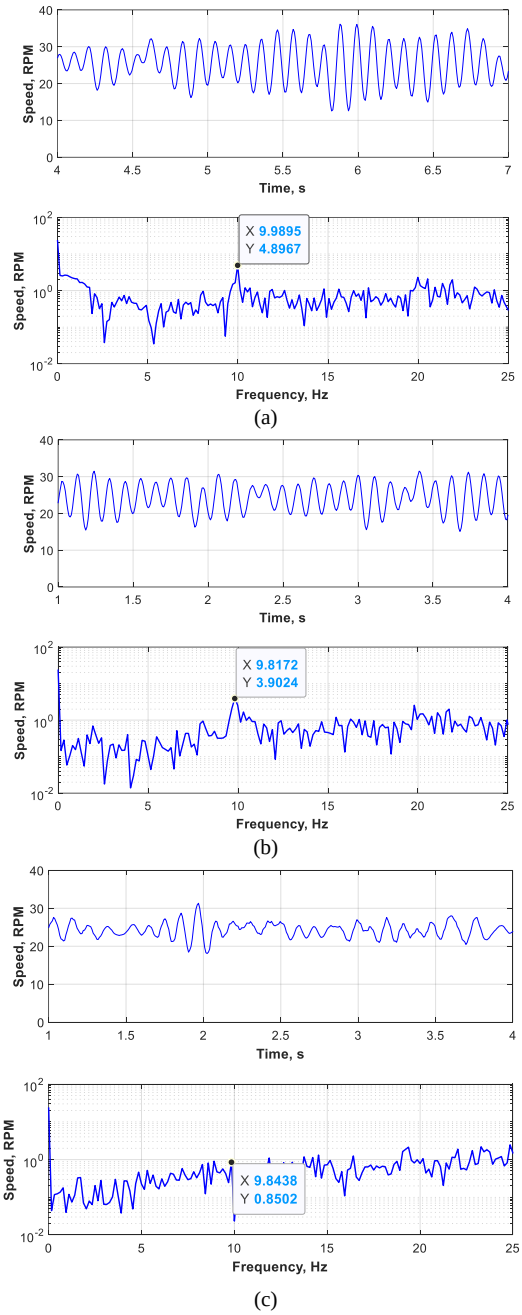

Fig. 18: Speed measurement at 25 RPM with 5 Nm average torque (on-vehicle): (a) PI (T_s = 5 ms) (b) PI (T_s = 1 ms) (c) PIR Controller.

Overall, several findings had been pointed out in this paper. Firstly, the natural frequency of the drivetrain will amplify the vibration when the torque ripple frequency close to the natural frequency. Secondly, increasing bandwidth with PI controller may cause the system goes unstable, as the noise rejection capability was reduced. Thirdly, PIR controller is still effective to be used in vehicle applications, even when the torque ripple is close to the drivetrain natural frequency.

The reduction in speed ripple or vibration by removing torque ripple at source using active control method will promote the uptake of PM machines in a wider range of applications, as this would increase the overall design flexibility.

REFERENCES

[1] Z. Q. Zhu, Y. Liu and D. Howe, "Minimizing the influence of cogging torque on vibration of PM brushless machines by direct torque control," *IEEE Trans. Magn.*, vol. 42, no. 10, pp. 3512–3514, Oct. 2006.

[2] M. J. Griffin, "Discomfort from feeling vehicle vibration," *Journal of Vehicle System Dynamics*, vol. 45, no. 7-8, pp. 679–698, Jun. 2007.

[3] X. Tang, J. Zhang, L. Zou, H. Yu, and D. Zhang, "Study on the torsional vibration of a hybrid electric vehicle powertrain with compound planetary power-split electronic continuous variable transmission," *Proceedings of the Institution of Mechanical Engineers, Part C: Journal of Mechanical Engineering Science*, vol. 228, no. 17, pp. 3107–3115, Jan. 2013.

[4] P. Drichel, M. Wegerhoff, R. Schelenz, and G. Jacobs, "Modeling an electric vehicle powertrain and analysis of vibration characteristics," *Torsional Vibration Symposium 2014*, Salzburg, Austria, May 2014.

[5] Q. Wang, K. Rajashekara, Y. Jia and J. Sun, "A real-time vibration suppression strategy in electric vehicles," *IEEE Trans. Veh. Technol.*, vol. 66, no. 9, pp. 7722–7729, Sep. 2017.

[6] F. Momen, K. Rahman, and Y. Son, "Electrical propulsion system design of Chevrolet Bolt battery electric vehicle," *IEEE Trans. Ind. Appl.*, vol. 55, no. 1, pp. 376–384, Jan.-Feb. 2019.

[7] J. Van Boekel, I. Besselink, and H. Nijmeijer, "Design and realization of a one-pedal-driving algorithm for the TU/e Lupo EL," *World Electric Vehicle Journal*, vol. 7, no. 2, pp. 226–237, Jun. 2015.

[8] M. Helmbrecht, C. Olaverri-Monreal, K. Bengler, R. Vilimek, and A. Keinath, "How electric vehicles affect driving behavioral patterns," *IEEE Intell. Transp. Syst. Mag.*, vol. 6, no. 3, pp. 22–32, Fall 2014.

[9] H. Kawamura, K. Ito, T. Karikomi, and T. Kume. "Highly-responsive acceleration control for the Nissan LEAF electric vehicle." SAE Technical Paper 2011-01-0350, 2011.

[10] J. Chen, "Vibration reduction in electric bus during acceleration and gear shifting," *Advances in Mechanical Engineering*, pp. 1–16, Mar. 2015.

[11] A. Mora, Á. Orellana, J. Juliet, and R. Cárdenas, "Model predictive torque control for torque ripple compensation in variable-speed PMSMs," *IEEE Trans. Ind. Electron.*, vol. 63, no. 7, pp. 4584–4592, Jul. 2016.

[12] G. H. Lee, W. C. Choi, S. I. Kim, S. O. Kwon, and J. P. Hong, "Torque ripple minimization control of permanent magnet synchronous motors for EPS applications," *International Journal of Automotive Technology*, vol. 12, no. 2, pp. 291−297, Apr. 2011.

[13] W. Qian, S. K. Panda, and J. Xu, "Torque ripple minimization in PM synchronous motors using iterative learning control," *IEEE Trans. Power Electron.*, vol. 19, no. 2, pp. 272–279, Mar. 2004.

[14] K. Nakamura, H. Fujimoto, and M. Fujitsuna, "Torque ripple suppression control for PM motor with high bandwidth torque meter," in *Proc. of ECCE 2009*, San Jose, CA, Sep. 2009, pp. 2572–2577.

[15] J. Xu, S. K. Panda, Y. Pan, T. Lee, and B. Lam, "A modular control scheme for PMSM speed control with pulsating torque minimization," *IEEE Trans. Ind. Electron.*, vol. 51, no. 3, pp. 526-536, Jun 2004.

[16] J. Böcker, N. Amann, B. Schulz, "Active suppression of torsional oscillations," *3rd IFAC Symposium on Mechatronic Systems*, Sydney, Austrilia, Sep. 2004.

[17] S. Chung, H. Kim, C. Kim, and M. Youn, "A new instantaneous torque control of PM synchronous motor for high-performance direct-drive applications," *IEEE Trans. Power Electron.*, vol. 13, no. 3, pp. 388–400, May 1998.

[18] J. Solsona, M. I. Valla, and C. Muravchik, "Nonlinear control of a permanent magnet synchronous motor with disturbance torque estimation," *IEEE Trans. Energy Convers.*, vol. 15, no. 2, pp. 163–168, Jun. 2000.

[19] S. Lee and H. Ahn, "Sensorless torque estimation using adaptive Kalman filter and disturbance estimator," in *Proc. of IEEE/ASME MESA 2010*, Qingdao, China, Jul. 2010, pp. 87–92.

[20] W. Wang, Y. Li, J. Shi, and C. Lin, "Vibration control method for an electric city bus driven by a dual motor coaxial series drive system based on model predictive control," *IEEE Access*, vol. 6, pp. 41188–41200, 2018.

[21] J. Licari, C. Ugalde-Loo, J. Ekanayake, and N. Jenkins, "Comparison of the performance and stability of two torsional vibration dampers for variable-speed wind turbines," *Journal of Wind Energy*, vol. 18, no. 10, pp. 1545–1559, Jun. 2015.

[22] C. Lai, G. Feng, K. Mukherjee, V. Loukanov, and N. C. Kar, "Torque ripple modeling and minimization for interior PMSM considering magnetic saturation," *IEEE Trans. Power Electron.*, vol. 33, no. 3, pp. 2417–2429, Mar. 2018.

[23] F. Bu *et al.*, "Speed ripple reduction of direct-drive PMSM servo system at low-speed operation using virtual cogging torque control method," *IEEE Trans. Ind. Electron.*, doi: 10.1109/TIE.2019.2962400.
[24] A. Houari *et al.*, "An effective compensation technique for speed smoothness at low-speed operation of PMSM drives," *IEEE Trans. Ind. Appl.*, vol. 54, no. 1, pp. 647–655, Jan.-Feb. 2018.
[25] J. Gao, X. Wu, S. Huang, W. Zhang, and L. Xiao, "Torque ripple minimisation of permanent magnet synchronous motor using a new proportional resonant controller," *IET Power Electron.*, vol. 10, no. 2, pp. 208–214, 10 2 2017.
[26] C. Xia, B. Ji, and Y. Yan, "Smooth speed control for low-speed high-torque permanent-magnet synchronous motor using proportional–integral–resonant controller," *IEEE Trans. Ind. Electron.*, vol. 62, no. 4, pp. 2123–2134, Apr. 2015.
[27] W. Qian, S. K. Panda, and J. X. Xu, "Speed ripple minimization in PM synchronous motor using iterative learning control," *IEEE Trans. Energy Conver.*, vol. 20, no. 1, pp. 53–61, Mar. 2005.
[28] A. Wojcik and T. Pajchrowski, "Torque ripple compensation in PMSM direct drive with position-based iterative learning control," in *Proc. of ME 2018*, Brno, Czech Republic, Dec. 2018, pp. 1–5.
[29] A. Abbaszadeh, D. Arab Khaburi, and J. Rodríguez, "Predictive control of permanent magnet synchronous motor with non-sinusoidal flux distribution for torque ripple minimisation using the recursive least square identification method," *IET Elec. PowerAppl.*, vol. 11, no. 5, pp. 847–856, 5 2017.
[30] A. G. de Castro, W. C. A. Pereira, T. E. P. de Almeida, C. M. R. de Oliveira, J. Roberto Boffino de Almeida Monteiro, and A. A. de Oliveira, "Improved finite control-set model-based direct power control of BLDC motor with reduced torque ripple," *IEEE Trans. Ind. Appl.*, vol. 54, no. 5, pp. 4476–4484, Sep.-Oct. 2018.
[31] D. Flieller, N. K. Nguyen, P. Wira, G. Sturtzer, D. O. Abdeslam, and J. Mercklé, "A self-learning solution for torque ripple reduction for nonsinusoidal permanent-magnet motor drives based on artificial neural networks," *IEEE Trans. Ind. Electron.*, vol. 61, no. 2, pp. 655–666, Feb. 2014.
[32] W. Xu, M. M. Ismail, Y. Liu, and M. R. Islam, "Parameter optimization of adaptive flux-weakening strategy for permanent-magnet synchronous motor drives based on particle swarm algorithm," *IEEE Trans. Power Electron.*, vol. 34, no. 12, pp. 12128–12140, Dec. 2019.
[33] S. Jung, J. Hong, and K. Nam, "Current minimizing torque control of the IPMSM using Ferrari's method," *IEEE Trans. Power Electron.*, vol. 28, no. 12, pp. 5603–5617, Dec. 2013.
[34] S. Morimoto, M. Sanada and Y. Takeda, "Effects and compensation of magnetic saturation in flux-weakening controlled permanent magnet synchronous motor drives," *IEEE Trans. Ind. Appl.*, vol. 30, no. 6, pp. 1632–1637, Nov. 1994.
[35] A. Rabiei, T. Thiringer, M. Alatalo, and E. A. Grunditz, "Improved maximum-torque-per-ampere algorithm accounting for core saturation, cross-coupling effect, and temperature for a PMSM intended for vehicular applications," *IEEE Trans. Transport. Electrific.*, vol. 2, no. 2, pp. 150–159, Jun. 2016.
[36] W. Huang, Y. Zhang, X. Zhang, and G. Sun, "Accurate torque control of interior permanent magnet synchronous machine," *IEEE Trans. Energy Convers.*, vol. 29, no. 1, pp. 29–37, Mar. 2014.
[37] D. W. Chung, and S. K. Sul, "Analysis and compensation of current measurement error in vector-controlled ac motor drives," *IEEE Trans. Ind. Appl.*, vol. 34, pp. 340–345, Mar./Apr. 1998.
[38] X. Tang, W. Yang, X. Hu, D. Zhang. "A novel simplified model for torsional vibration analysis of a series-parallel hybrid electric vehicle," *Journal of Mechanical Systems and Signal Processing*, vol. 85, pp. 329–338, Feb. 2017.
[39] M. Mauri, M. Rossi, and M. Bruha, "Generation of torsional excitation in a variable-speed-drive system," in *Proc. of SPEEDAM 2016*, Anacapri, Italy, Jun. 2016, pp. 516–521.
[40] B. T. Boulter, "Applying drive performance specifications to systems applications. I. Speed performance," *IEEE Trans. Ind. Appl.*, vol. 37, no. 4, pp. 1082–1087, Jul.-Aug. 2001.
[41] J. G. Ziegler and B. N. Nancy. "Optimum settings for automatic controllers," *Journal of Dynamic Systems Measurement and Control-Transactions of The ASME*, vol. 115, pp. 220–222, 1942.
[42] J. M. Rodríguez, R. Meneses, and J. Orús, "Active vibration control for electric vehicle compliant drivetrains," in *Proc. of IECON 2013*, Vienna, Austria, Nov. 2013, pp. 2590–2595.

Hawwooi Chuan received the B.Eng. degree in electrical engineering from the University of Malaya, Kuala Lumpur, Malaysia, in 2012, the M.Sc. degree from Durham University, Durham, U.K., in 2013, and the Ph.D. degree from the University of Edinburgh, Edinburgh, U.K. in 2018, respectively.

From July 2018 to August 2019, he was with the Institute for Advanced Automotive Propulsion Systems (IAAPS), Department of Mechanical Engineering, University of Bath, Bath, U.K., as a Research Associate. His research interests are in electrical machine drives and control system.

Seyed Mahdi Fazeli received the Ph.D. degree from the University of Malaya, Kuala Lumpur, Malaysia, in 2013. He is currently working as Researcher with the Institute for Advanced Automotive Propulsion Systems (IAAPS), University of Bath, Bath, U.K.

His main research interests include power electronic converters, variable-speed ac drives, Electric vehicle, and nonlinear control. He is a member of the Institution of Engineering and Technology and is a Chartered Engineer.

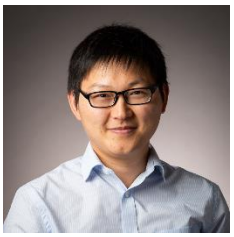

Zhongze Wu (S'15-M'18) received the B.Eng. and M.Sc. degrees in electrical engineering from Southeast University, Nanjing, China, in 2010 and 2013, respectively, and the Ph.D. degree in electrical and electronic engineering from The University of Sheffield, Sheffield, U.K., in January 2017.

Since August 2018, he has been with the Institute for Advanced Automotive Propulsion Systems (IAAPS), Department of Mechanical Engineering, University of Bath, Bath, U.K., where he is currently a Lecturer. His major research interests include the advanced electrical machines and drives for electric propulsion systems.

From January 2017 to August 2018, he was with Warwick Manufacturing Group (WMG), University of Warwick, Coventry, U.K., as a research fellow in electrical machines.

Richard Burke received the M.Eng. degree in Automotive Engineering and the Ph.D. degree from the University of Bath, Bath, U.K., in 2008 and 2011, respectively. He is currently a Senior Lecturer within the Institute for Advanced Automotive Propulsion Systems (IAAPS) and a Director of the EPSRC Centre for Doctoral Training in Advanced Automotive Propulsion Systems at University of Bath, Bath, U.K.

His research interests are in the system level interactions that occur under transient operating conditions with propulsion systems. He is a Fellow of the IMechE.